Studies on characterization, magnetic and electrochemical properties of nano-size pure and mixed ternary transition metal ferrites prepared by the auto-combustion method

M. Khairy[1,2,a)], W. A. Bayoumy[1], S. S. Selima[1], M. A. Mousa[1]

[1]Chemistry Department, Faculty of Science, Benha University, Benha 13511, Egypt
[2]Chemistry Department, College of Science, Imam Mohammad Ibn Saud Islamic University, Riyadh 11461, Saudi Arabia
[a)]Address all correspondence to this author. e-mail: mohkhairy@fsc.bu.edu.eg, moh_khairy3@yahoo.com

Nanocrystallites of pure and mixed ternary ferrites, $NiFe_2O_4$ (NiF), $CuFe_2O_4$ (CuF), $CoFe_2O_4$ (CoF), $Ni_{0.5}Cu_{0.5}Fe_2O_4$ (CuNiF), $Ni_{0.5}Co_{0.5}Fe_2O_4$ (NiCoF), and $Cu_{0.5}Co_{0.5}Fe_2O_4$ (CuCoF) were prepared using the auto-combustion method employing urea as a fuel. The obtained materials were investigated by Fourier transform infrared spectroscopy (FTIR), X-ray diffraction (XRD), transmission electron miscroscopy (TEM), scanning electron microscopy (SEM), and BET techniques. The elemental composition of the prepared samples was checked by X-ray fluorescence (XRF) analysis. XRD indicated that the as-synthesized samples exhibit a pure spinel crystal structure. The samples have crystallite sizes ranged from 12 to 47 nm. SEM and TEM analyses showed almost spherical morphology for all ferrite particles. The M–H curves recorded using the VSM (vibrating sample magnetometer) technique showed ferromagnetic hysteresis loop for all the samples investigated. The ferrite samples were tested to be used as a supercapacitor electrode material. It is found that the measured specific capacitance of the ferrite electrodes increases according to CuCoF > NiCoF > CoF > NiCuF > CuF > NiF. The CuCoF sample showed the greatest specific capacitance of 220 F/g at discharging current density *I* of A/g with, an energy density of 34.72 Wh/kg and power density of 605 W/kg. The magnetic properties were also measured for the obtained nanoparticles.

Introduction

Ferrite nanoparticles have drawn significant consideration and a lot of works continue to study them due to their significance in the high-density information storage, microwave industries, ferrofluids, catalysis, magnetic resonance imaging (MRI), magnetic refrigeration systems, etc. [1,2]. The mixed spinel ferrites have the common formula of $(M^{2+}_{1-x}Fe^{3+}_x)_A$ $[M_xFe^{3+}_{2-x}]_BO_4$, which represent tetrahedral (A) and octahedral (B) sites, respectively, M symbolizes ions of divalent, and *x* signifies the inversion extent (outlined the portion of the sites of (A) engaged by Fe^{3+} ion).

The motivating and advantageous of ferrites magnetic properties hang on the selection of divalent cations and their spreading between tetrahedral (A) and octahedral (B) sites of the spinel matrix [3,4,5]. The distribution of cations based on numerous aspects, such as ionic radii and electronic configuration. This allocation has a considerable effect on the microstructure and the physical properties of the ferrites and in turn their applications.

$NiFe_2O_4$ as one of the precious ferrites has a cubic spinel inverse structure whereby half of the Fe^{3+} ions resides in the tetrahedral sites and Ni^{2+} resides in the octahedral site. It displays a ferromagnetic behavior and exhibits high theoretical specific electrical capacitance, apparent redox behavior, and low price [6,7,8].

$CoFe_2O_4$ has been broadly studied because of superior chemical stability, its high electromagnetic operation, and mechanical hardness, which nominate it as an appropriate applicant for the electronic components operated in computers, magnetic cards, and recording devices [9,10].

$CuFe_2O_4$ with an inverse spinel structure has been broadly used in electronics and catalysts. It has been considered as an encouraging material for electrochemical capacitors as a consequence of its high theoretical capacity (895 mAh/g) and low price [11].
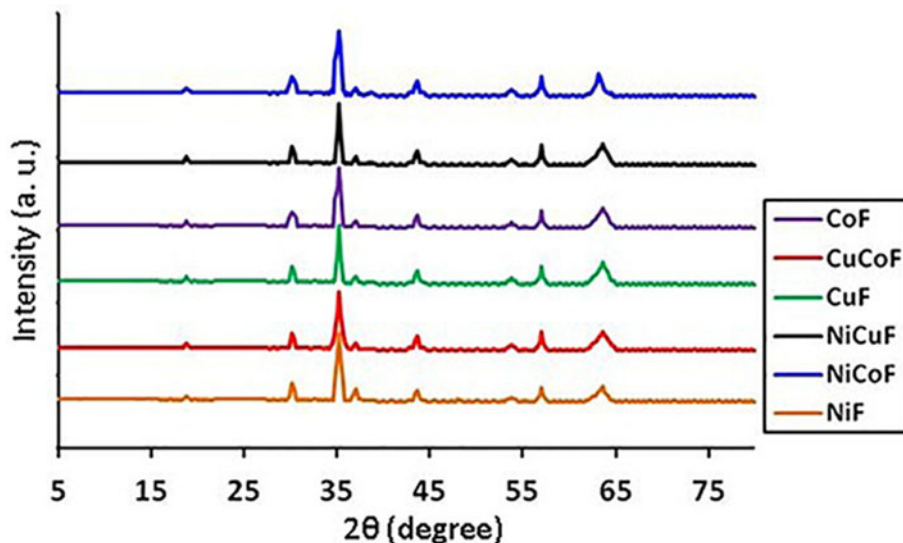
Figure 1: XRD of the investigated ferrites.

The properties of these transition metal ferrites are dependent on the chemical arrangement and microstructural features, which can be regulated in the manufacture and production procedures. Therefore, it is valuable for studying the appropriateness of mixed ferrites in the magnetic topic as well in supercapacitors as possible electrode materials exhibit high capacitance value. This is attributed to the presence of several redox states. According to that, we synthesized nano ferrites of $NiFe_2O_4$ (NiF), $CuFe_2O_4$ (CuF), $CoFe_2O_4$ (CoF), $Ni_{0.5}Cu_{0.5}Fe_2O_4$ (NiCuF), $Ni_{0.5}Co_{0.5}Fe_2O_4$ (NiCoF), and $Cu_{0.5}Co_{0.5}Fe_2O_4$ (CuCoF), using a combustion method. In general, the synthesis by the combustion technique has been chosen because of its excellent ability in the preparation of the ferrites [12,13]. The method is very easy because several steps are not involved.

The structural and surface texture properties of the prepared samples are characterized by using X-ray diffraction (XRD), Fourier transform infrared spectroscopy (FTIR), X-ray fluorescence (XRF), scanning electron microscopy (SEM), transmission electron miscroscopy (TEM), and Brunauer-Emmett-Teller (BET) surface area analysis techniques. The magnetic and electrochemical properties have been studied using Vibrating sample magnetometer (VSM), cyclic voltammetry (CV), charging–discharging (CD), and Electrochemical impedance spectroscopy (EIS) techniques.

Results and discussion

X-ray diffraction

The XRD patterns of the investigated materials are shown in Fig. 1. The XRD data of the as-synthesized materials demonstrate a pattern of ferrites peaks at approximately 30.5, 36.1, 37.3, 43.5, 53.5, 57.1, and 63.5 which can be assigned to

(220), (311), (222), (400), (422), (511), and (440) crystal planes, respectively. These peaks approve the creation of the spinel cubic structure, with the JCPDS card (25-0283) for $CuFe_2O_4$, JCPDS card (22-1086) for $CoFe_2O_4$, and JCPDS card (10-0325) for $NiFe_2O_4$. The shifting in the diffraction peak angles refers to the formation of tensile stress, whereas the shifting in the direction of higher angles denotes compressive stress [14]. The strain along the [311] direction has been estimated using the following:

$$\Delta d/d = \frac{d_{\text{ferrite}} - d_{\text{CoF}}}{d_{\text{CoF}}}, \qquad (1)$$

where Δd is the change in the d-spacing relative to the pure CoF sample. A compressive strain is observed in CuF, NiF, NiCoF, CuCoF, and NiCoF samples due to the substitution of Cu^{2+} or Ni^{2+} with small ionic radii in place of Co^{2+} ion: the ionic radii of Cu^{2+} (0.73 Å) and Ni^{2+} (0.70 Å) is less than Co^{2+} (0.745 Å). The obtained results are recorded in Table 1.

Because all the XRD measurements are performed under the same conditions, thus the crystalline quality of our ferrites can be evaluated by determining the crystallinity degree (N_c) using the following equation:

$$N_c = \frac{I_{\text{ferrite}} - I_{\text{CoF}}}{I_{\text{CoF}}}, \qquad (2)$$

where I_{ferrite} is the integrated intensity for all ferrites except CoF and I_{CoF} is the integrated intensity for pure CoF. A positive value of N_c points to the improvement in the crystallinity balanced with the CoF and the negative value denotes the loss in crystallinity. The obtained results are listed in Table 1 and found that the crystallinity increases in the order: NiF > CuF > NiCuF > CoF > NiCoF > CuCoF.

TABLE 1: FTIR and powder XRD data of ferrite samples for the most intense (311) reflection peak.

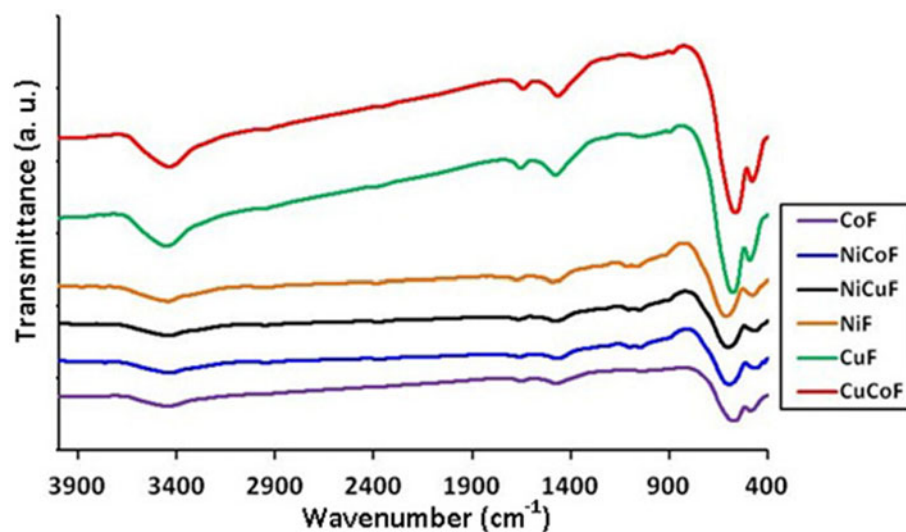| Sample	Lattice constant (Å)	XRD particle size (nm)	TEM particle size (nm)	Lattice strain $\times 10^{-3}$	Crystallinity	ν_1 (cm^{-1})	ν_2 (cm^{-1})
CoF	8.382	25	24	–	–	571	465
CuCoF	8.372	14	12	13.60	−0.713	564	490
CuF	8.370	44	41	13.46	−0.475	575	477
NiF	8.344	49	47	13.35	0.1232	584	484
NiCoF	8.368	21	18	13.51	0.1232	593	487
NiCuF	8.362	34	30	13.41	0.2312	600	494

Figure 2: FTIR of the investigated ferrites.

The crystallite sizes (D_{XRD}) of the ferrite samples were estimated by Scherrer's equation [15] using the most intense peak (311) of XRD:

$$D_{XRD} = 0.9\lambda/\beta \cos\theta, \qquad (3)$$

where β is the peak width at half-maximum intensity, λ is the wavelength of the K_α of Cu target (λ = 0.154 nm). It was found that the obtained ferrites samples have nano-sized crystallites in the range of 14–49 nm (Table 1). This reveals that the urea can be considered here as good fuel for preparing nano ferrite materials and the dispersion medium for starting reactants.

The lattice parameters calculated for investigated ferrites are found to be 8.382, 8.372, 8.370, 8.344, 8.368, and 8.362 Å for CoF, CuCoF, CuF, NiF, NiCoF, and NiCuF, respectively. It can be seen that with introducing Cu or Ni in the ferrite composition, the lattice constant and unit cell volume decrease due to decreasing the ionic radii of these ions comparable with that of Co^{2+} ion.

FTIR studies

The spectra of FTIR of the investigated materials are revealed in Fig. 2. The vibration band (ν_1) (564–610 cm^{-1}) corresponding to the tetrahedral sites vibrations of spinel ferrites and (ν_2) (465–498 cm^{-1}) corresponding to the stretching vibrations of octahedral sites of spinel ferrites [16,17]. These bands are the characteristic of inverse spinel ferrites [18]. FTIR spectra also display an absorption band at ~1648 cm^{-1}, matching to the carbonyl group (C=O) stretching vibration, correlated to the urea molecule. FTIR spectral data are summarized in Table 1. The change in band position on going from one composition to others might be attributed to variation in the inter-nuclear distance of Fe^{3+}–O^{2-} in the equivalent lattice sites [19]. The presence of long shoulder at the band of the tetrahedral site is due to the existence of other ionic states in this site [20].

Chemical composition, SEM and TEM images

The morphology and particle size of the investigated ferrites are analyzed by TEM and SEM micrographs, revealed in Figs. 3(A) and 3(B). SEM image [Fig. 3(B)] reveals that the surface images of the samples show cavities and pores shaped by avoiding the gas throughout the combustion reaction. The communication of clusters produces macropores which permit the moving of electrolyte, thus generating a big surface area for redox reactions [21]. Nanopores can be also noted on the surfaces of the clusters, with size variable with the composition of the
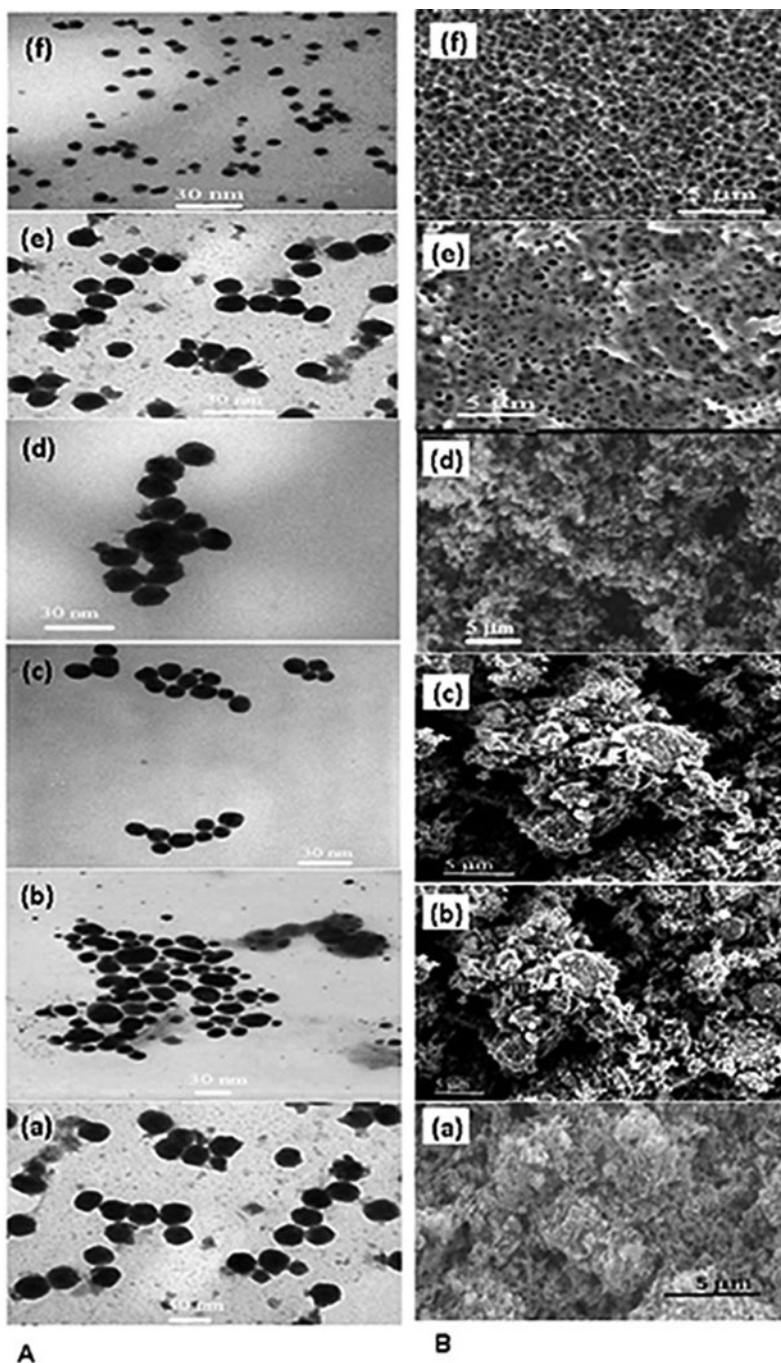
Figure 3: (A) TEM images of (a) NiF, (b) CuF, (c) CoF, (d) NiCuF, (e) NiCoF, and (f) CuCoF. (B) SEM images of (a) NiF, (b) CuF, (c) CoF, (d) NiCuF, (e) NiCoF, and (f) CuCoF.

materials. These pores are valuable because they deliver comfortable channel for ion transfer at the electrode–electrolyte interface (see Section Electrochemical study). The elemental composition of the ferrites analyzed by XRF techniques shows the composition agree well with the suggested ferrite composition (Table 2).

The TEM micrographs [Fig. 3(A)] show more-or-less spherical particle shapes with some clustering/agglomeration between them. The average particle sizes obtained from TEM images are listed in Table 1. The particle sizes found by the

Sherrer's equation disagree to some extent than that defined from TEM images (Table 1). This might be due to the distinctive handle of two techniques.

Surface textural properties

The isothermal N_2 adsorption–desorption of the ferrite samples are illustrated in Fig. 4. The sorption isotherms show an isotherm of type IV and V according to the IUPAC classifications [22] and corresponding to a mesoporous structure. The

TABLE 2: Composition obtained from XRF data, textural surface data, and hysteresis loop parameters of the synthesized ferrites.

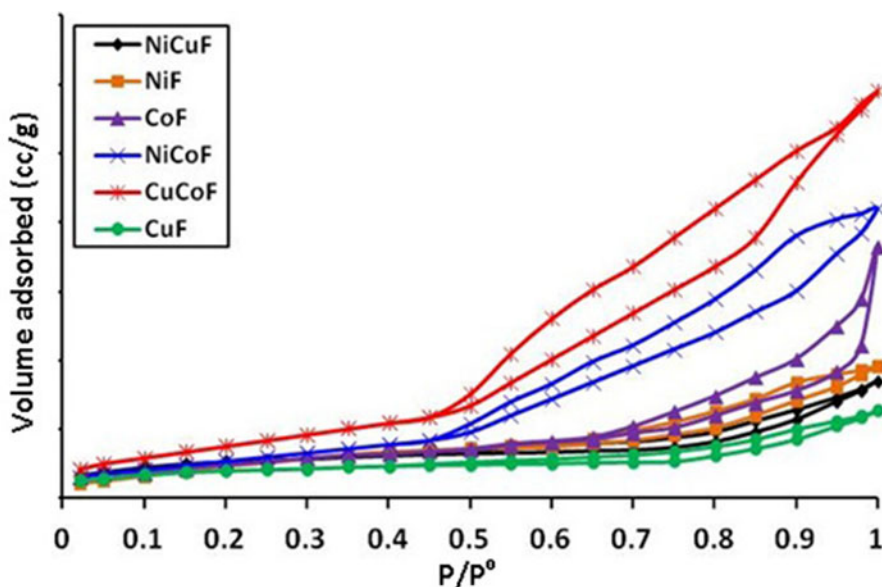| Sample	Cu (wt%)	Ni (wt%)	Co (wt%)	Fe (wt%)	Particle size (nm)	Surface area (m²/g)	Pore volume (nm)	M_s (emu/g)	H_c (Oe)	M_r (emu/g)	M_r/M_s
CuF	26.53	–	–	46.61	41	54	4.9	9.7	240	5.1	0.52
NiF	–	25.07	–	47.62	47	46	4.7	29.7	250	16.86	0.55
CoF	–	–	25.01	47.7	24	70	5.8	44.9	340	19.6	0.43
NiCuF	13.35	12.29	–	47.2	30	68	5.8	12.1	250	5.41	0.44
CuCoF	13.44	–	12.36	47.11	12	91	6.1	20.2	300	9.12	0.45
NiCoF	–	12.51	12.47	47.55	18	78	6.0	36.3	335	15.1	0.45

Figure 4: N₂ adsorption–desorption of the investigated ferrites.

clear hysteresis loops are noted in the higher range of relative pressure, signifying to the presence of macropores. The hysteresis loop of CuCoF, NiCoF, CoF, and NiF are H3 type referring to the slit-shaped pores generated between the plate-like particles, whereas in the case of CuF and NiCuF, it is H1 type corresponding to well-defined cylindrical pore channels. Textural parameters obtained from nitrogen adsorption–desorption isotherm data are summarized in Table 2. The surface area and pore size (determined using the Barrett–Joyner–Halend (BJH) distribution method) were found to increase with reducing the particle size and follow the order: CuCoF > NiCoF > CoF > NiCuF > CuF > NiF.

Magnetic studies

The magnetic properties of the studied ferrites have been investigated using VSM in a magnetic field of 10 kOe. For each sample, a hysteresis loop with a standard S-shape type is obtained (Fig. 5). Similar behavior was also detected for the nano ferrite particles prepared by others using different techniques [23,24, 25,26,27,28,29]. The size and shape of hysteresis curves for a magnetic material are of vital practical importance. The

width and the degree of contraction of the hysteresis loop are found to vary with the sample composition. The magnetic parameters gotten from the hysteresis loops are shown in Table 2. The saturation magnetization values (M_s) for the nano CuFe, NiFe, and CoFe were found considerably less than that for their bulk materials (33.4, 55, and 80 emu/g, respectively), which can be attributed to the surface spin. The reduction in these parameters could be attributed to the presence of spin canting [30]. Fundamentally, several mechanisms have been proposed to describe the source of spin canting: one is based on the surface and interfaces impact [31,32]. According to this mechanism, the particles are assumed to be arranged in a ferrimagnetically structured core and a spin-disordered surface layer, and a combination of the two constituents is recognized through exchange interactions. Dissimilarities of coordination numbers and gap of surface cations could decrease the atomic magnetic moment of discrete sublattices causing a reduction in the average hyperfine field of surface cations. Consequently, the reduction in the grains, the increase in the portion of surface cation and the minor of the whole hyperfine field directed to the match reduction in the saturation magnetization.
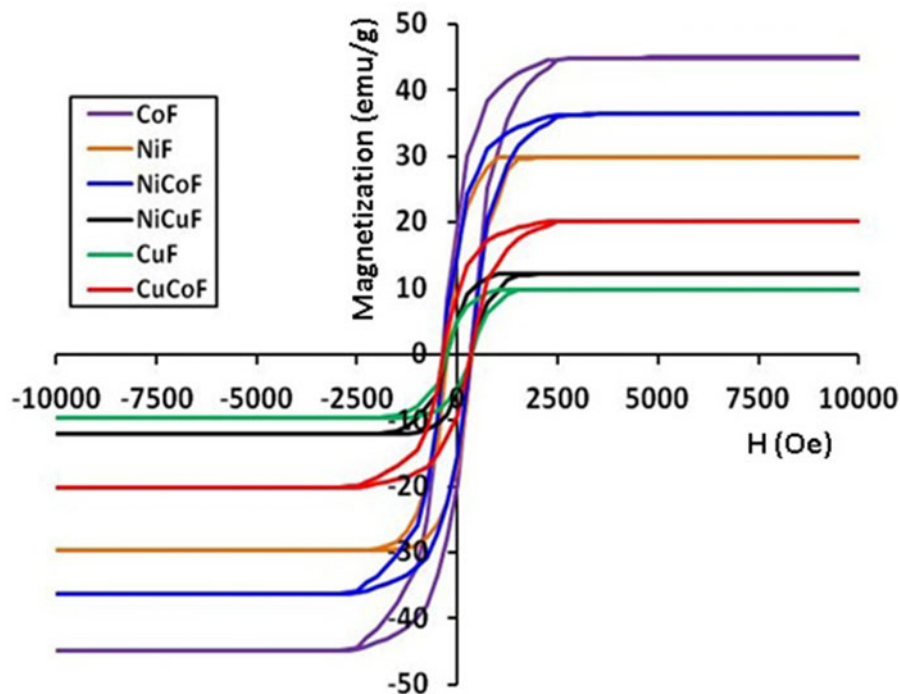
Figure 5: Magnetic hysteresis of the investigated ferrites.

The saturation magnetization (M_s) based on the constituent metal ions distribution on cationic (A and B) sites and their relative interactions can be determined from A site (μ_A) and B site (μ_B) magnetic moments [33]. Our results also show that the saturation magnetization (M_s) of the ferrites enlarge with increasing cobalt content (9.7, CuF; 29.7, NiF; 20.2, CuCOF; and 36.3, NiCoF). This is due to the presence of a large number of cobalt ions with a higher magnetic moment value (with 3 μB per ion) in the octahedral sites (B sites) compared with the number of nickel or copper ions with lower magnetic moment values with 2 and 1 μ_B per ion, respectively. This results in an increase in the magnetic moment of B site as well as increasing in A–B interactions. The net magnetic moment of 3 μ_B per formula unit for $CoFe_2O_4$ and 2 μ_B per formula unit for $NiFe_2O_4$ as well as 1 μ_B per formula unit for $CuFe_2O_4$ are due to Fe^{3+} (with 5 μ_B per ion) in the spinel structure is consistently dispersed among octahedral and tetrahedral sites.

On the other hand, increasing the Cu content in both NiF and CoF leads to decreasing the value of M_s (29.7, NiF; 44.9, CoF; 12.1, NiCuF; and 20.2, CuCoF). This is attributed to the higher copper ions ratio with a lower magnetic moment value (1 μ_B per ion) in the octahedral sites at the expense of the nickel and cobalt ions of higher magnetic moment values with 2 and 3 μ_B per ion, respectively.

The coercivity value (H_c) was also found to rise with increasing Co concentration (240, CuF; 250, NiF; 300, CuCOF; and 35, NiCoF). This might be attributed to the cobalt cations have the greater magnetocrystalline anisotropy contrasted to Ni and Cu cations [34,35,36]. It has been registered

that cobalt-doped nickel ferrite has more M_s and H_c values than those for nickel ferrite [37]. Analogous outcomes were found by Skomski and Sellmyer [38]. The values of the squareness ratio of CoF, NiCoF, CuCoF, and NiCuF samples are below 0.5 clearly shows that these samples are multidomain in nature.

The obtained magnetic parameters (saturation magnetization—M_s, coercivity—H_c, and Remanence—M_r) of our binary or ternary samples are found to be much larger than the reported value of other related oxides such as $NiFe_2O_4$ ($M_s = 28.82$ emu/g, $H_c = 82.85$ Oe, and $M_r = 1.42$ emu/g) [39]. It also exceeds the values of $CuFe_2O_4$ annealed at 350 °C ($M_s = 0.0744$ emu/g, $H_c = 231.04$ Oe, and $M_r = 0.0009$ emu/g) [40], $CuFe_2O_4$ NPs ($M_s = 11.6$ emu/g, $H_c = 152.7$ Oe, and $M_r = 2.3$ emu/g) [41], $CoFe_2O_4$ ($M_s = 31.6$ emu/g, $H_c = 870$ Oe, and $M_r = 9.6$ emu/g) [42], $CoFe_2O_4$ ($M_s = 38.58$ emu/g and $H_c = 53.59$ Oe) [43], other ternary mixed spinels such as $Ni_{0.4}Cu_{0.6}Fe_2O_4$ ($M_s = 9$ emu/g, $H_c = 657$ Oe, and $M_r = 4$ emu/g) [44], $Ba_{0.4}Cu_{0.6}Fe_2O_4$ ($M_s = 5.31$ emu/g, $H_c = 18$ Oe, and $M_r = 1.44$ emu/g) [45], $Ru_{0.02}Cu_1Fe_{1.98}O_4$ ($M_s = 6.81$ emu/g, $H_c = 166.59$ Oe, and $M_r = 1.09$ emu/g) [46], $Co_{0.25}Sr_{0.05}Zn_{0.7}Fe_2O_4$ ($M_s = 13.1$ emu/g, $H_c = 5.1$ Oe, and $M_r = 0.01$ emu/g) [47], and $Co_{0.5}Zr_{0.5}Fe_2O_4$ ($M_s = 34.06$ emu/g and $M_r = 10.78$ emu/g) [48].

Electrochemical study

The electrical capacitance of the investigated ferrite electrodes in the 3 M KCl electrolyte solution was determined *via* a CV
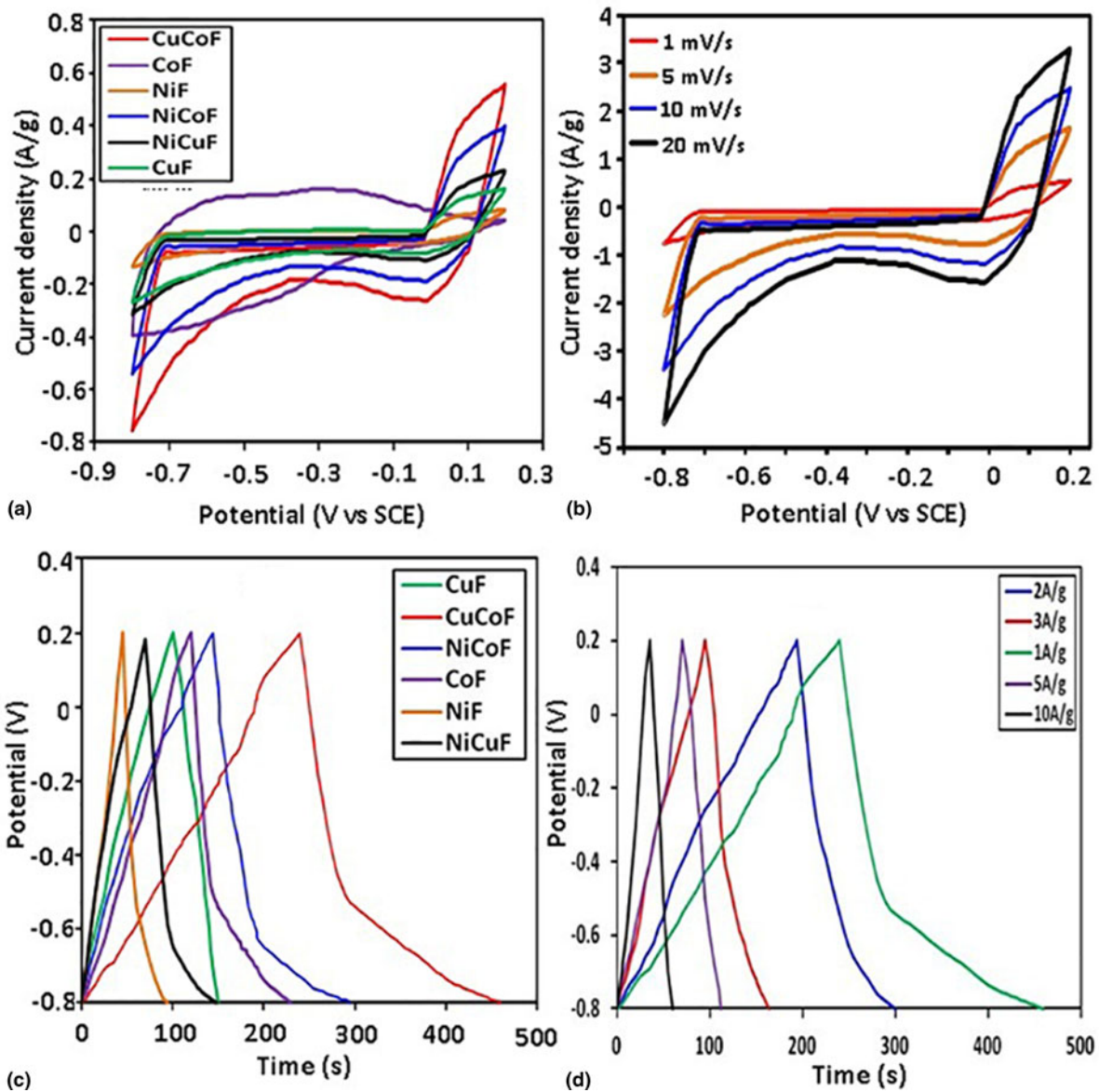
Figure 6: (a) CV of investigated electrodes at 1 mV/s in 3 M KCl. (b) CV of CuCoF at different scan rates. (c) CD plots of the investigated ferrites using current density of 1 A/g. (d) CD of CuCoF electrode at different current densities.

technique. Figure 6(a) demonstrates the results obtained in the range of potential of −0.8 to 0.2 V with a scan rate of 1 mV/s. The specific capacitance (C_{sp}) of the electrodes have been calculated from the following equation [49]:

$$C_{sp} = \frac{1}{vw(\Delta V)} \int_{Va}^{Vc} iV dV, \qquad (4)$$

where v is the scan rate (1 mV/s), ΔV (V) is the drop potential, and w (g) is the electrode mass. The CV profile shows a capacitive behavior with nearly a rectangular shape, denoting a reversible system. The calculated C_{sp} values are given in Table 3. The capacitance increases in the following order:

CuCoF > NiCoF > CoF > NiCuF > CuF > NiF. The increase in the capacitance of the mixed ferrites comparable with the pure ones may be due to the synergistic effects of the mixed components.

The highest capacitance in CuCoF can be also ascribed to its high surface area and the smaller ionic radius. The CuCoF with the highest capacitance was further investigated at several scan rates between 1 and 20 mV/s and the outcomes are illustrated in Fig. 6(b). As the scan rate increases, the CV curves area increases referring to an ideal capacitive behavior [50].

The specific capacitances at the different scan rates were also calculated using Eq. (4) and found to be 250, 180, 113, and 75 F/g, at scan rates of 1, 5, 10, and 20 mV/s, respectively.

TABLE 3: Electrochemical data of the studied samples.

Sample	C_{sp} (F/g) CV, 1 mV/s	C_{sp} (F/g) CD, 1 A/g	ESR (ohm)	R_t (ohm)	Energy density (Wh/kg)	Power density (W/kg)
CuF	56	50	1.61	4.71	7.77	550
CoF	118	110	1.52	5.51	16.38	536
NiF	49	44	2.30	4.31	6.81	490
CuCoF	250	220	1.71	1.82	34.72	545
			(190)		26.38	545
NiCuF	84	77	1.79	5.71	11.66	551
NiCoF	160	151	2.01	1.85	22.22	555

(···) C_{sp} at current density 10 A/g.

The reduction development of the capacitance indicates that the fractions of the electrode surface are unreachable at a high scan rate. Lessen scan rate causes extra time for ions to get into the bulk of the ferrite.

Figure 6(c) illustrates the CD curves of the investigated ferrites at a current density of 1 A/g with a voltage between −0.8 and 0.2 V. The internal resistance of the electrodes causes an IR drop for all curves [51]. The lowest internal resistance is achieved by the CuCoF sample referring to good electrode material connection with the collector and, thus, exhibits the highest C_{sp} value compared to those of the other electrodes. The specific capacitances gained from the CD plots at a current density of 1 A/g (Table 3) are in agreement with those acquired from the CV plots.

The obtained results show that the increase in the replacement of Ni^{+2} ions with Co^{2+} ions in the spinel structure causes an increase in the specific capacitance values (50 F/g, CuF; 44 F/g, NiF; 220 F/g, CuCoF; and 151 F/g, NiCoF). This might be attributed to the replacing of Ni^{2+} ions with Co^{+2} ion, in the octahedral sites of the spinel structure causing an increase in the lattice parameter and a decrease the cationic bond length because the radius of Co^{+2} ions is larger than that of Ni^{+2} ions. This strengthened the interaction of Co^{+2} ions with O^{-2} ions, leading to the splitting of egt_{2g} levels to egt_{2g} sublevels [52]. So, the specific capacitance increases, when the available ways for the electrode to react with the electrolyte increase [52].

The galvanostatic of the ferrite electrode with high capacitance (CuCoF) at several current densities of 1, 2, 3, 5, and 10 A/g were studied under an applied potential of −0.2 to 0.8, and the results obtained are illustrated in Fig. 6(d). At a high current density (10 A/g), the C_{sp} value of the CoCuF ferrite is found to be lower than those at lower current density (Table 3).

It is significant notifying that the specific capacitance of the our binary or ternary mixed oxides samples are higher that those reported by others such as SC CoFe$_{0-5}$ (77.8 F/g at 1 A/g) [53], CoFe$_2$O$_4$||GO ASC (31.3 F/g at 5 mV/s) [54], NiCoFe$_2$O$_4$ (50 F/g at 1 A/g) [55], NiCuFe$_2$O$_4$ (44 F/g at 1 A/g) [55], CuCoFe$_2$O$_4$ (76.9 F/g at 1 A/g) [55],
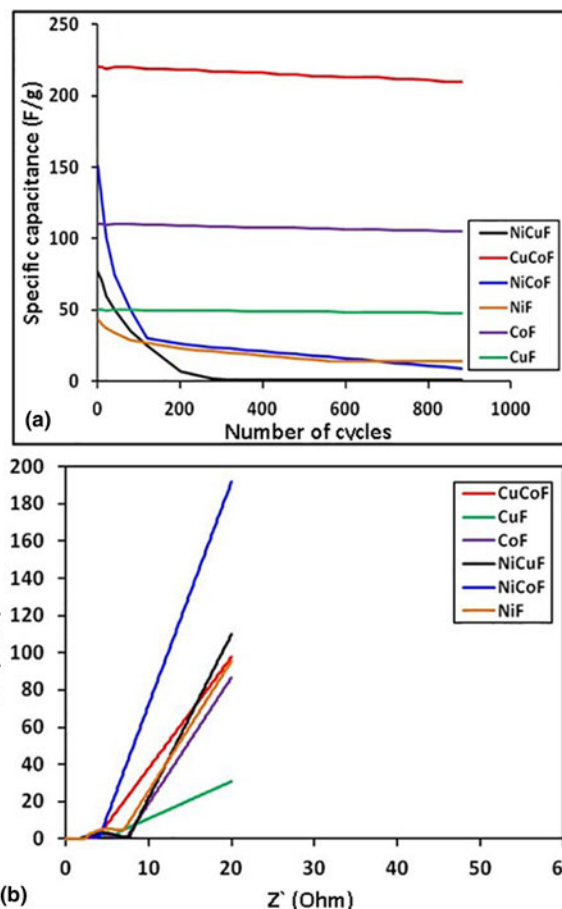

Figure 7: (a) Capacitance stability of the investigated electrodes. (b) Nyquist plots of the investigated ferrite electrodes.

Co$_{0.8}$Ni$_{0.2}$Fe$_2$O$_4$ (22.2 10 mV/s) [56], NiCoFe$_2$O$_4$ (17 F/g at 5 mV/s) [57], and NiCuFe$_2$O$_4$ (47 F/g at 10 mV/s) [57].

The stability of the investigated ferrite electrodes was studied for 1000 cycles at an applied current density of 1 A/g and is illustrated in Fig. 7(a), which shows a variation in C_{sp} with a cycle number. The capacitive retention of the electrodes shows the order: CuCoF > CoF > CuF > NiF > NiCuF > NiCoF. The CuCoF electrode decreases by ∼6% over 1000 cycles. The lessening observed in specific capacitance with the increase in the number of cycles may be attributed to the loss of active material in the electrodes.

The power density (P, W/kg) and average energy density (E, Wh/kg) of the electrochemical capacitors are estimated according to the following equations [58]:

$$E = \frac{1000C_s \times \Delta V^2}{2 \times 3600}, \quad (5)$$

$$P = \frac{E \times 3600}{\Delta t}, \quad (6)$$

where Δt (s) is the time of discharge and ΔV is the active potential window. The outcomes gotten are given in Table 3.

EIS was studied to show the electrical resistance and the capacitance trend of the electrodes. Figure 7 illustrates Nyquist plots for all the investigated samples with a half circle and slanting line at high-frequency and low-frequency regions, respectively. The half circle is attributed to resistance of charge transfer (CT) at the active material interface implied that supercapacitors required an blocking conduct [59]. The low-frequency slanting line characteristics for the Warburg element. It is indicated that the process of transfer of the electrolyte ions is the diffusion process and refers to electrocapacitive behavior. Figure 7(b) shows that the diameter of semi-circles of the electrode material follows the order: NiCuF > CoF > CuF > NiF > NiCoF > CuCoF, which represents the order of the CT rate in the electrode material. Meanwhile, the slope of the straight lines become more vertical in the order: CuCoF > NiCoF > NiCuF > NiF > CoF > CuF, indicating the order of better capacitance behavior which is reliable with the results of CD and CV. In other words, the slanting line in the region of low frequency in the studied ferrites, especially for CuCoF, is a great evidence for perfect capacitive performance with a small resistance of diffusion of ions in the electrode material. This can be attributed to the facilities with which the ions in the electrolyte move in a mesoporous surface. The equivalent series resistance (ESR) values are acquired starting with an x-intercept of the Nyquist plot and are listed in Table 3.

Conclusions

In our work, nanocrystalline of pure copper ferrite, cobalt ferrite, nickel ferrite, and mixed of them were prepared by the self-combustion method. Structural, compositional, magnetic, and electrochemical behavior of the prepared samples were well studied by FTIR, XRD, XRF, TEM, SEM, BET, VSM, CV, and CD techniques. XRD results approved the construction of a pure spinel structure of the prepared ferrites. TEM, SEM micrographs, and BET analysis pointed to the formation of a porous structure that allows electrolyte ions to pass easily. The obtained samples display ferromagnetism nature for all samples at room temperature with apparent hysteresis loops, revealing the possibility of their use as high-density magnetic storage and medical diagnostic, etc. The electrochemical results showed that the capacitance values follow the following order: CuCoF > NiCoF > CoF > NiCuF > CuF > NiF with the highest specific capacitance of 220 F/g for CuCoF with an energy density of 34.7 Wh/kg and power density of 605 W/kg. The cation distribution in the studied samples revealed the dominant influence on the structural, optical, magnetic, and electrochemical properties of the obtained ferrites. The present study shows that the combustion procedure can be operated to create a broad range of ferrite nanoparticles useful for different applications such as magnetic materials and energy storage devices.

Experimental

Preparation method

Materials used are reagent grades and used without further purifications for preparing the ferrites by the combustion procedure. The materials employed in this work were urea, cobalt nitrate $[Co(NO_3)_2 \cdot 6H_2O]$, ferric nitrate $[Fe(NO_3)_3 \cdot 9H_2O]$, and nickel nitrate $[Ni(NO_3)_2 \cdot 6H_2O]$. The stoichiometric combinations of the above materials were dissolved in distilled water. Urea was added to the solution until the precipitate was produced, then placed in an oven overnight at 115 °C. Finally, the precursor was completely ignited in a muffle furnace for 4 h at 600 °C to create the corresponding ferrites.

Characterization methods

The as-synthesized samples were confirmed by a D8 Bruker AXS analytical XRD technique (Massachusetts, United States) using Cu K_α radiation and Cu/Ni filter to investigate their crystal structure. The FTIR spectrum of each specimen was carried out by using a Brucker FT IR (Massachusetts, United States) at the wavenumbers of 4000–400 cm^{-1}. Morphologies and structural characteristics of the as-synthesized samples were determined by TEM (JEOL-2010) (Japan) and SEM (JEOL JEM-100CXII) (Japan) techniques. The elemental composition was determined using an HNU ED-XRF analyzer (Munich, Germany). The surface texturing of samples was measured via N_2 adsorption/desorption by the volumetric technique via an ASAP-2020 surface area 180 analyzer. Vibrating sample magnetometer model (VSM-9600M-1, USA) was used to investigate the magnetic characteristics of the prepared samples in the applied field with maximum of 10 kOe.

Electrochemical properties measurements

Electrochemical capacities were calculated using a system consisting from three electrode in 3 M KCl electrolyte at room temperature, using saturated calomel and Pt square foil (area = 0.61 cm^2) as a reference electrode and a counter electrode, respectively. The working electrode was made by mixing 8 mg of the ferrite sample, 1.5 mg of carbon black, and 1 mg of polytetrafluorethylene (5% wt) to get a homogeneous slurry. The slurry was coated onto the precleaned Indium Tin Oxide (ITO) conducting glass and dried at 320 K for 24 h. The electrochemical performance was studied by applying the electrochemical techniques: CV, CD, and EIS using a Gamry G750 potentiostat/galvanostat instrument (Pennsylvania, United States) with the EIS300 software.

References

1. **S. Hazra and N.N. Ghosh**: Preparation of nanoferrites and their applications. *J. Nanosci. Nanotech.* **14**, 1983 (2014).

2. **Y. Gao, Z. Wang, J. Pei, and H. Zhang**: Structure and magnetic properties correlated with cation distribution of Ni0.5-xMoxZn0.5Fe2O4 ferrites prepared by sol-gel auto-combustion method. *Ceram. Int.* **44**, 20148 (2018).

3. **H. Yanagihara, S. Sharmin, T. Niizeki, and E. Kita**: Magnetic properties of spinel ferrite thin films grown by reactive sputtering. *Mater. Trans.* **57**, 777 (2016).

4. **V.D.d. Oliveira, R.M. Rubinger, M.R.d. Silva, A.F. Oliveira, and G. Rodrigues**: Magnetic and electrical properties of $Mn_xCu_{1−x}Fe_2O_4$ ferrite. *Mater. Res.* **19**, 786 (2016).

5. **J. Li, H. Yuan, G. Li, Y. Liu, and J. Leng**: Cation distribution dependence of magnetic properties of sol-gel prepared $MnFe_2O_4$ spinel ferrite nanoparticles. *J. Magn. Magn. Mater.* **322**, 3396 (2010).

6. **P.R. Kumar and S. Mitra**: Nickel ferrite as a stable, high capacity and high rate anode for Li-ion battery applications. *RSC Adv.* **3**, 25058 (2013).

7. **M. Islam, G. Ali, M.G. Jeong, W. Choi, K.Y. Chung, and H.-G. Jung**: Study on the electrochemical reaction mechanism of $NiFe_2O_4$ as a high-performance anode for Li-Ion batteries. *ACS Appl. Mater. Interface* **9**, 14833–14843 (2017).

8. **F. Wu, X. Wang, M. Li, and H. Xu**: A high capacity $NiFe_2O_4$/ RGO nanocomposites as superior anode materials for sodium-ion batteries. *Ceram. Int.* **42**, 16666 (2016).

9. **H. Gao, S. Liu, Y. Li, E. Conte, and Y. Cao**: A critical review of spinel structured iron-cobalt oxides based materials for electrochemical energy storage and conversion. *Energies* **10**, 1787 (2017).

10. **J. Yin, L. Shen, Y. Li, and M. Lu**: $CoFe_2O_4$ nanoparticles as efficient bifunctional catalysts applied in Zn–air battery. *J. Mater. Res.* **33**, 590 (2018).

11. **W. Zhang, B. Quan, C. Lee, S.-K. Park, X. Li, E. Choi, G. Diao, and Y. Piao**: One-step facile solvothermal synthesis of copper ferrite-graphene composite as a high-performance supercapacitor material. *ACS Appl. Mater. Interfaces* **7**, 2404 (2015).

12. **P. Sivakumar, R. Ramesh, A. Ramanand, S. Ponnusamy, and C. Muthamizhchelvan**: Preparation and properties of nickel ferrite ($NiFe_2O_4$) nanoparticles via sol-gel auto-combustion method. *Mater. Res. Bull.* **46**, 2204 (2011).

13. **A.C.F.M. Costa, E. Tortella, M.R. Morelli, M. Kaufman, and R.H.G.A. Kiminami**: Effect of heating conditions during combustion synthesis on the characteristics of $Ni_{0.5}Zn_{0.5}Fe_2O_4$ nanopowders. *J. Mater. Sci.* **37**, 3569 (2002).

14. **M.R. Panigrahi and S. Panigrahi**: Structural analysis of 100% relative intense peak of $Ba_{1−x}Ca_xTiO_3$ ceramics by X-ray powder diffraction method. *Physica B* **405**, 1787 (2010).

15. **H.P. Klug and L.E. Alexander**: *X-ray Diffraction Procedures for Polycrystalline and Amorphous Materials* (Wiley, New York, 1970).

16. **T.T. Srinivasan, C.M. Srivastava, N. Venkataramani, and M.J. Patini**: Infrared absorption in spinel ferrites. *Bull. Mater. Sci.* **6**, 1063 (1984).

17. **R.P. Patil, S.D. Delekar, D.R. Mane, and P.P. Hankare**: Synthesis, structural and magnetic properties of different metal ion substituted nanocrystalline zinc ferrite. *Results Phys.* **3**, 129 (2013).

18. **İ. Şabikoğlua, L. Paralı, O. Malina, P. Novak, J. Kaslik, J. Tucek, J. Pechousek, J. Navarik, and O. Schneeweiss**: The effect of neodymium substitution on the structural and magnetic properties of nickel ferrite. *Prog. Nat. Sci. Mater. Int.* **25**, 215 (2015).

19. **V. Rathod, A. V. Anupama, R V. Kumar, V. M. Jali, and B Sahoo**: Correlated vibrations of thetetrahedral and octahedral complexes and splitting of the absorption bands inFTIR spectra of Li-Zn ferrites. *Vib.Spectrosc.* **92**, 267 (2017).

20. **A. Pradeep, P. Priyadharsini, and G. Chandrasekaran**: Sol gel route of Synthesis of nanoparticles of $MgFe_2O_4$ and XRD, FTIR and VSM study. *J. Magn. Magn. Mater.* **320**, 2774 (2008).

21. **B. Bhujun, M.T.T. Tan, and A.S. Shanmugam**: Study of mixed ternary transition metal ferrites as potential electrodes for supercapacitor applications. *Results Phys.* **7**, 345 (2017).

22. **F.J. Sotomayor, A.K. Cychosz, and M. Thommes**: Characterization of micro/mesoporous materials by physisorption: Concepts and case studies. *Acc. Mater. Surf. Res.* **3**, 34 (2018).

23. **M. Khan, W. Khalid, and A. Mumtaz**: Magnetic characterization of $Co_{1−x}Ni_xFe_2O_4$ (0⩽x⩽1) nanoparticles prepared by co-precipitation route. *Physica E* **41**, 593 (2009).

24. **N.B. Velhal, N.D. Patil, A.R. Shelke, N.G. Deshpande, and V.R. Puri**: Structural, dielectric and magnetic properties of nickel substituted cobalt ferrite nanoparticles: Effect of nickel concentration. *AIP Adv.* **5**, 097166 (2015).

25. **K.S. Rao, G.S.V.R.K. Choudary, K.H. Rao, and C. Sujatha**: Structural and magnetic properties of ultrafine $CoFe_2O_4$ nanoparticles. *Proc. Mater. Sci.* **10**, 19 (2015).

26. **S. Muthurani, M. Balaji, S. Gautam, K.H. Chae, J.H. Song, D.P. Padiyan, and K. Asokan**: Magnetic and humidity sensing properties of nanostructured $Cu_xCo_{1−x}Fe_2O_4$ synthesized by autocombustion technique. *J. Nanosci. Nanotechnol.* **11**, 5850 (2011).

27. **S. Akhter, D.P. Paul, M.A. Hakim, S. Akhter, S.M. Hoque, and H.N. Das**: Magnetic properties of $Cu_{1−x}Zn_xFe_2O_4$ ferrites with the variation of zinc concentration. *J. Mod. Phys.* **3**, 398 (2012).

28. **M.A. Zinovik and E.V. Zinovik**: Ferrites with rectangular and square hysteresis loops. *Powder Metall. Met. Ceram.* **44**, 66 (2005).

29. **A.M. Mohammad, S.M. Aliridh, and T.H. Mubarak**: Structural and magnetic properties of Mg-Co ferrite nanoparticles. *Dig. J. Nanomater. Bios.* **13**, 615 (2018).

30. D. Peddis, N. Yaacoub, M. Ferretti, and D. Fiorani: Cationic distribution and spin canting in $CoFe_2O_4$ nanoparticles. *J. Phys. Condens. Matter* **23**, 426004 (2011).

31. M. Darbandi, F. Stromberg, J. Landers, N. Reckers, B. Sanyal, W. Keune, and H. Wende: Nanoscale size effect on surface spin canting in iron oxide nanoparticles synthesized by the microemulsion method. *J. Phys. D. Appl. Phys.* **45**, 195001 (2012).

32. H.Y. Hwang, Y. Iwasa, M. Kawasaki, B. Keimer, N. Nagaosa, and Y. Tokura: Emergent phenomena at oxide interfaces. *Nat. Mater.* **11**, 103 (2012).

33. K. Pubby, K.V. Babu, and S.B. Narang: Magnetic, elastic, dielectric, microwave absorption and optical characterization of cobalt-substituted nickel spinel ferrites. *Mater. Sci. Eng. B* **255**, 114513 (2020).

34. S.R. Naik and A.V. Stalker: Change in the magnetostructural properties of rare earth doped cobalt ferrites relative to the magnetic anisotropy. *J. Mater. Chem.* **22**, 2740 (2012).

35. K. Raju and D.H. Yoon: Structural and magnetic properties of Zn and Co substituted nickel ferrites prepared by the citrate sol–gel method. *J. Supercond. Nov. Magn.* **27**, 1285 (2014).

36. P. Bruno and J.-P. Renard: Magnetic surface anisotropy of transition metal ultrathin films. *Appl. Phys. A* **49**, 499 (1989).

37. **J. P. Mallick: Comparative study of the structure & magnetic properties of nickel cobalt ferrites synthesized by solid-state & auto-combustion processing techniques. Thesis, Department of Ceramic Engineering, National Institute of Technology, Rourkela, 2011.**

38. R. Skomski and D.J. Sellmyer: Handbook of advanced magnetic materials. *Adv. Magn. Mater.* **1**, 30 (2005).

39. H. Moradmard, S.F. Shayesteh, P. Tohidi, Z. Abbas, and M. Khaleghi: Structural, magnetic and dielectric properties of magnesium doped nickel ferrite nanoparticles. *J. Alloys Compd.* **650**, 116 (2015).

40. S. Pavithradevi, N. Suriyanarayanan, and T. Boobalan: Synthesis, structural, dielectric and magnetic properties of polyol assisted copper ferrite nano particles. *J. Magn. Magn. Mater.* **426**, 137 (2017).

41. R.S. Yadav, J. Havlica, J. Masilko, L. Kalina, J. Wasserbauer, M. Hajdúchová, V. Enev, I. Kuřitka, and Z. Kožáková: Cation migration-induced crystal phase transformation in copper ferrite nanoparticles and their magnetic property. *J. Supercond. Nov. Magn.* **29**, 759 (2016).

42. A. Mazrouei and A. Saidi: Microstructure and magnetic properties of cobalt ferrite nano powder prepared by solution combustion synthesis. *Mater. Chem. Phys.* **209**, 152 (2018).

43. B. Purnama, A.T. Wijayanta, and Suharyana: Effect of calcination temperature on structural and magnetic properties in cobalt ferrite nano particles. *J. King Saud Univ. Sci.* **31**, 956 (2019).

44. J. Balavijayalakshmi, N. Suriyanarayanan, and R. Jayaprakash: Role of copper on structural, magnetic and dielectric properties of nickel ferrite nanoparticles. *J. Magn. Magn. Mater.* **385**, 302 (2015).

45. U. Naresh, R.J. Kumar, and K.C.B. Naidu: Hydrothermal synthesis of barium copper ferrite nanoparticles: Nanofiber formation, optical, and magnetic properties. *Mater. Chem. Phys.* **236**, 121807 (2019).

46. V. Manikandana, V. Kuncserb, B. Vasilec, S. Kavitad, S. Vigneselvane, and R.S. Manef: Enhancement in magnetic and dielectric properties of the ruthenium-doped copper ferrite ($RuCuFe_2O_4$) nanoparticles. *J. Magn. Magn. Mater.* **476**, 18 (2019).

47. P. Imanipour, S. Hasani, M. Afshari, S. Sheykh, A. Seifoddini, and K. Jahanbani-Ardakani: The effect of divalent ions of zinc and strontium substitution on the structural and magnetic properties on the cobalt site in cobalt ferrite. *J. Magn. Magn. Mater.* **510**, 166941 (2020).

48. S. Kavitha and M. Kurian: Effect of zirconium doping in the microstructure, magnetic and dielectric properties of cobalt ferrite nanoparticles. *J. Alloys Compd.* **799**, 147 (2019).

49. D. Han, P. Xu, X. Jing, J. Wang, P. Yang, Q. Shen, J. Liu, D. Song, Z. Gao, and M. Zhang: Trisodium citrate assisted synthesis of hierarchical NiO nanospheres with improved supercapacitor performance. *J. Power Sources* **235**, 45 (2013).

50. Z. K Ghouri, N. A. M. Barakat, and H. Y. Kim: Synthesisand Electrochemical Properties of MnO2 and Co-Decorated Graphene asNovel Nanocomposite for Electrochemical Super Capacitors Application. *Energy and Environ. Focus* **4**, 34 (2015).

51. M.S. Javed, S. Dai, M. Wang, D. Guo, L. Chen, X. Wang, C. Hu, and Y. Xi: High-performance solid-state flexible supercapacitor based on molybdenum sulfide hierarchical nanospheres. *J. Power Sources* **285**, 63 (2015).

52. S. Sharifi, A. Yazdani, and K. Rahimi: Effect of Co^{2+} content on supercapacitance properties of hydrothermally synthesized $Ni_{1-x}Co_xFe_2O_4$ nanoparticles. *Mater. Sci. Semicond. Proc.* **108**, 104902 (2020).

53. S. Martinez-Vargasa, A.I. Mtz-Enriquezb, H. Flores-Zuñigac, A. Encinasc, and J. Olivac: Enhancing the capacitance and tailoring the discharge times of flexible graphene supercapacitors with cobalt ferrite nanoparticles. *Synth. Metals* **264**, 116384 (2020).

54. K.V. Sankar, R.K. Selvan, and D. Meyrick: Electrochemical performances of $CoFe_2O_4$ nanoparticles and a rGO based asymmetric supercapacitor. *RSC Adv.* **5**, 99959 (2015).

55. B. Bhujun, M.T. Tan, and A.S. Shanmugam: Study of mixed ternary transition metal ferrites as potential electrodes for supercapacitor applications. *Results Phys.* **7**, 345 (2017).

56. **I. Shakira, A. Rasheedc, S. Haiderd, and M.F.A. Aboud**: The Impact of Cu^{2+} and Mg^{2+} onto the electrochemical energy storage properties of nanocrystalline $Co_{0.8}Ni_{0.2}Fe_2O_4$ particles and their hybrids with graphene. *Ceram. Intern.* **45**, 18099 (2019).

57. **B. Bhujun, M.T. Tan, and A.S. Shanmugam**: Study of mixe ternary transition metal ferrites as potential electrodes for supercapacitor applications. *Results Phys.* **7**, 345 (2017).

58. **F. Ran, X. Zhang, Y. Liu, K. Shen, X. Niu, Y. Tan, L. Kong, L. Kang, C. Xu, and S. Chen**: Super long-life supercapacitor electrode materials based on hierarchical porous hollow carbon microcapsules. *RSC Adv.* **5**, 87077 (2015).

59. **M.A. Mousa, M. Khairy, and M. Shehab**: Nanostructured ferrite/graphene/polyaniline using for supercapacitor to enhance the capacitive behavior. *J. Solid State Electrochem.* **21**, 995 (2017).